

Topological Directional Coupler

Yandong Li,^{1,*} Minwoo Jung,² Yang Yu,¹ Yuchen Han,² Baile Zhang,^{3,4} and Gennady Shvets^{1,†}

¹*School of Applied and Engineering Physics, Cornell University, Ithaca, New York, 14853, USA*

²*Department of Physics, Cornell University, Ithaca, New York, 14853, USA*

³*Division of Physics and Applied Physics, School of Physical and Mathematical Sciences, Nanyang Technological University, 21 Nanyang Link, Singapore, 637371, Singapore*

⁴*Centre for Disruptive Photonic Technologies, The Photonics Institute, Nanyang Technological University, 50 Nanyang Avenue, Singapore, 639798, Singapore*

(Dated: December 1, 2023)

Interferometers and beam splitters are fundamental building blocks for photonic neuromorphic and quantum computing machinery. In waveguide-based photonic integrated circuits, beam-splitting is achieved with directional couplers that rely on transition regions where the waveguides are adiabatically bent to suppress back-reflection. We present a novel, compact approach to introducing guided mode coupling. By leveraging multimodal domain walls between microwave topological photonic crystals, we use the photonic-spin-conservation to suppress back-reflection while relaxing the topological protection of the valley degree of freedom to implement tunable beam splitting. Rapid advancements in chip-scale topological photonics suggest that the proposed simultaneous utilization of multiple topological degrees of freedom could benefit the development of novel photonic computing platforms.

Neuromorphic [1] and quantum [2, 3] computing procedures involve a variety of linear algebra operations on a set of N -dimensional unitary matrices $[U(N)]$. Such operations can be carried out using basic photonic devices — phase shifters and beam splitters. Specifically, an arbitrary N dimensional linear operation can be realized with $N(N-1)/2$ Mach-Zehnder interferometers (MZIs) [4–6]. Although it is challenging to perfectly align all the photonic elements with a free-space optical setup when N becomes large, with guided-wave implementations enabled by modern integrated photonics techniques, all elements can be squeezed on a chip, thus motivating the development of large-scale MZI arrays [7–9]. However, key components of MZIs, directional couplers, sacrifice compactness to minimize the photon loss because the coupled waveguides need long (tens of wavelengths) transition regions to prevent unwanted back-reflections [10].

Topological photonics offers new strategies for light manipulation, particularly suppressing back-reflections [11–13]: the immediate result of topological protection is granted by the conservation of the relevant topological index. For example, first-order \mathbb{Z} and \mathbb{Z}_2 indices (e.g., the Chern, spin-Chern, and valley-Chern numbers) guarantee robust propagation of edge states [14–17] at the domain walls between two topologically distinct bulks of photonic crystals (PhCs) with overlapping band gaps. Applications of topological photonics have also been extended to maintaining the robustness of few-photon quantum states [18–21].

Inspired by the semiconductor pioneer H. Kroemer’s famous phrase, “the interface is the device” [22], we aim to design compact directional couplers by utilizing multimodal topological interfaces that support edge modes characterized by more than one topological index [23]. One candidate for the bulk PhC is a spin photonic crystal

(SPC) [15, 24, 25], whose band gaps are characterized by half-integer spin and valley Chern numbers $C_{s,v} = \pm 1/2$, where $s \in \{\uparrow, \downarrow\}$ and $v \in \{\mathbf{K}, \mathbf{K}'\}$ label the spin and valley degrees of freedom (DoFs), respectively. A domain wall between two SPCs with opposite spin Chern numbers supports two chiral topological edge states in each valley. Their propagation direction is locked to the spin DoF and protected from backscattering by the conservation of the spin DoF. On the other hand, the valley DoF depends on the direction of the domain wall: $\mathbf{K}(\mathbf{K}')$ valleys are well-defined at zigzag domain walls, and the two co-propagating edge states (one per valley) are protected against inter-valley scattering [17, 26, 27].

When the protection of the valley DoF is intentionally broken in a controlled manner such that the spin DoF remains conserved, the two co-propagating states can crosstalk without experiencing backscattering. Such intentional breaking of some (but not all) topological DoFs offers an opportunity for creating topological directional couplers (TDCs). Harnessing the topological protection to suppress backscattering can potentially make TDCs smaller than their conventional counterparts because (a) the transition regions [10] between coupled waveguides become unnecessary; (b) The strong modal overlap between the two valley-polarized states reduces the required length of the crosstalking region. In other words, photonic spin conservation enables unidirectional propagation; Valley hybridization causes a significant (non-evanescent) coupling between the two valley-polarized states and enables a short coupling length. In this Letter, we demonstrate that by arranging the domain wall along the armchair direction and engineering its properties, inter-valley scattering is induced [17, 28–30] in a controllable way, which enables a compact, tunable TDC.

We use the microwave SPCs introduced in Ref. [24, 27]

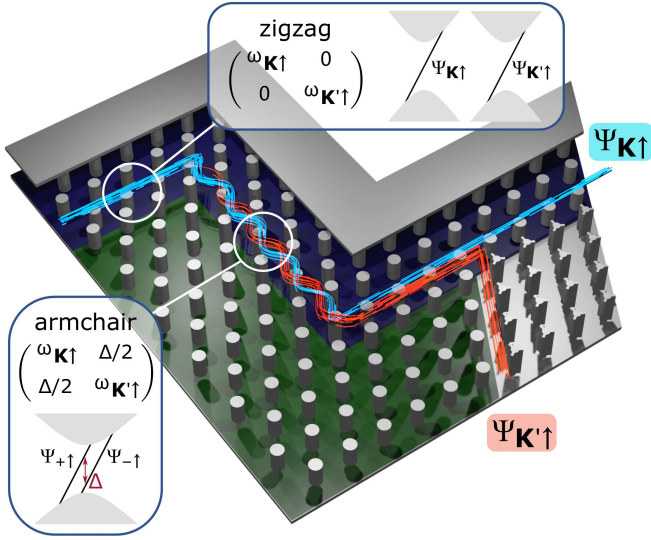


FIG. 1. Topological directional coupler based on a designer domain wall between SPCs. Green (blue) regions: $\text{SPC}^{1(2)}$, metallic rods are attached to the top (bottom) metal plate. The input state $\Psi_{\mathbf{K}\uparrow}$ is injected in a zigzag domain wall, where the valley DoF is conserved. Along the armchair domain wall, the valley basis $\Psi_{\mathbf{K}(\mathbf{K}')\uparrow}$ hybridizes into $\Psi_{+(-)\uparrow}$. The bottom right gray region: VPC for routing valley-polarized modes for detection. Insets: Along the zigzag domain wall, \mathbf{K} and \mathbf{K}' valleys are separated in the k -space, and inter-valley scattering is negligible. The edge-state Hamiltonian is hence diagonal; Along the armchair domain wall, \mathbf{K} and \mathbf{K}' valleys are folded to the Γ point, resulting in a strong inter-valley scattering, and the off-diagonal components in the edge-state Hamiltonian become nonzero.

to implement such a TDC. As depicted in Fig. 1, the structure is based on the domain wall between $\text{SPC}^{1(2)}$, triangular lattices of metallic rods attached to the top (bottom) radiation-confining metallic plates. The photonic spin DoF is synthesized by mixing the TE- and TM-polarized modes, which is accomplished by breaking the reflection symmetry about the mid-height x - y plane [24]. The $\text{SPC}^{1,2}$ possess spin-Chern numbers $C_s^{(1,2)} = \mp 1/2$, accordingly (where the superscript (1) corresponds to $-1/2$ for spin up and $1/2$ for spin down). Details of the physical setup are described in the Supplementary Material. We judiciously arrange the $\text{SPC}^{1,2}$ and let them form a domain wall with a 90° turning corner – the domain wall is zigzag-type before, and armchair-type after the turn (Fig. 1). Along zigzag domain walls, the discrete translational symmetry along one of the primitive lattice vector directions (\mathbf{a}_1 or \mathbf{a}_2) is conserved, and therefore the valley DoF is conserved. In contrast, armchair domain walls are along the $\mathbf{a}_1 + \mathbf{a}_2$ direction, thus changing the discrete translational symmetry and folding both valleys to the Γ point ($k = 0$).

For the zigzag domain wall, the edge-state Hamiltonian is diagonal in the valley basis, $(\Psi_{\mathbf{K}\uparrow}, \Psi_{\mathbf{K}'\uparrow})^T$, because the two valleys are well-separated in the k -space.

When an arbitrary spin-up mode $\Psi_\uparrow = \cos(\theta/2)\Psi_{\mathbf{K}\uparrow} + e^{i\varphi}\sin(\theta/2)\Psi_{\mathbf{K}'\uparrow}$ is guided into or excited in the zigzag domain wall, the proportion of the $\mathbf{K}(\mathbf{K}')$ valley-polarization, which is the modulus squared projection onto the valley-basis, $P_{\mathbf{K}(\mathbf{K}')\uparrow}^{\text{zig}}(l) \equiv |\langle \Psi_\uparrow^{\text{zig}}(l) | \Psi_{\mathbf{K}(\mathbf{K}')\uparrow} \rangle|^2$, is independent of the propagation distance l ,

$$\begin{aligned} P_{\mathbf{K}\uparrow}^{\text{zig}}(l) &= \cos^2 \theta/2, \\ P_{\mathbf{K}'\uparrow}^{\text{zig}}(l) &= \sin^2 \theta/2. \end{aligned} \quad (1)$$

Here, only the spin-up modes are considered because the spin-down ones exit the structure after excitation.

On the other hand, for the armchair domain wall, the edge state Hamiltonian can be represented as $H_{\text{arm}} = (\omega_0, \Delta/2; \Delta/2, \omega_0)$, where $\omega_0 \equiv \omega_{\mathbf{K}\uparrow} = \omega_{\mathbf{K}'\uparrow}$, because the two Dirac cones at the \mathbf{K} and \mathbf{K}' valleys are gapped through the same mechanism. The off-diagonal terms $\Delta/2$ represent the \mathbf{K} - \mathbf{K}' valley hybridization due to inter-valley scattering. When Ψ_\uparrow enters the armchair domain wall, its time-evolution is governed by the operator $e^{-iH_{\text{arm}}l/v_g}$. Hence, Ψ_\uparrow experiences a Rabi oscillation, and the proportion of the $\mathbf{K}(\mathbf{K}')$ valley polarization, $P_{\mathbf{K}(\mathbf{K}')\uparrow}^{\text{arm}}(l) \equiv |\langle \Psi_\uparrow^{\text{arm}}(l) | \Psi_{\mathbf{K}(\mathbf{K}')\uparrow} \rangle|^2$, becomes

$$\begin{aligned} P_{\mathbf{K}\uparrow}^{\text{arm}}(l) &= \cos^2(\theta/2) \cos^2[\Phi(\Delta)] + \sin^2(\theta/2) \sin^2[\Phi(\Delta)], \\ P_{\mathbf{K}'\uparrow}^{\text{arm}}(l) &= \cos^2(\theta/2) \sin^2[\Phi(\Delta)] + \sin^2(\theta/2) \cos^2[\Phi(\Delta)], \end{aligned} \quad (2)$$

where $\Phi(\Delta) \equiv l\Delta/(2v_g)$. Hence, the armchair domain wall rotates Ψ_\uparrow in the valley basis.

In order to measure the two proportions $P_{\mathbf{K}(\mathbf{K}')\uparrow}(L)$ at the end of the armchair domain wall of length $l = L$, we first restore the valley-DoF-conservation. We let the domain wall make another 90° turn, and the armchair domain wall out-couples to a zigzag one, along which valley-conservation ensures that $P_{\mathbf{K}(\mathbf{K}')\uparrow}(L)$ remains unchanged. Then, we joint a valley photonic crystal (VPC) with the two SPCs to form two single-mode topological waveguides (Fig. 1), and each waveguide supports only one valley-polarization for the spin-up mode [24, 31]. Therefore, the two valley-polarizations are separated, and $P_{\mathbf{K}(\mathbf{K}')\uparrow}(L)$ can be calculated by measuring the output energy of the two single-mode waveguides [25].

To summarize our design, the engineered domain wall performs two changes-of-basis. The guided edge mode basis changes from $(\Psi_{\mathbf{K}\uparrow}, \Psi_{\mathbf{K}'\uparrow})^T$ to $(\Psi_{+\uparrow}, \Psi_{-\uparrow})^T$ [here $\Psi_{\pm\uparrow} \equiv (\Psi_{\mathbf{K}\uparrow} \pm \Psi_{\mathbf{K}'\uparrow})/\sqrt{2}$], and back to $(\Psi_{\mathbf{K}\uparrow}, \Psi_{\mathbf{K}'\uparrow})^T$ again, corresponding to the three different types of domain walls: zigzag SPC^1 - SPC^2 , armchair SPC^1 - SPC^2 , and zigzag $\text{SPC}^{1,2}$ -VPC. This design realizes a unitary transformation, $e^{-iH_{\text{arm}}L/v_g}$, on valley-polarized topological edge modes, $\Psi_{\mathbf{K}(\mathbf{K}')\uparrow}$. The form of this unitary transformation offers two tuning knobs: one is L , the length of the armchair domain wall, which, however, requires significant changes of the structure dimension. The other is the degree of inter-valley scattering, which is represented by Δ in the off-diagonal entries of H_{arm} and can

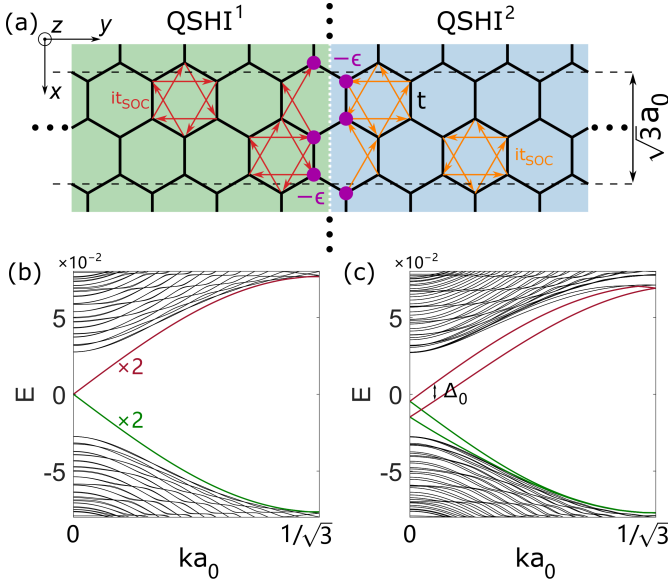


FIG. 2. The tight-binding model. (a) Schematic of the armchair domain wall between two 2D quantum spin Hall insulators (QSHIs). In the green (blue) region, we implement clockwise (counterclockwise) next nearest neighbor (NNN) hoppings [red (orange) arrows] for spin up. For spin down, the NNN hoppings are reversed. The atomic sites adjacent to the domain wall are perturbed with the on-site potential $-\epsilon$ (purple dots). (b,c) Band diagrams of the armchair domain wall with the perturbation (b) $\epsilon = 0$ and (c) $|\epsilon| = 0.42|t|$. In (b), the spin up (down) modes are doubly degenerate. $|t|$ is the nearest neighbor hopping strength.

be tuned by varying unit cell parameters in the vicinity of the domain wall.

The inter-valley scattering amplitude is sensitive to detailed changes along the armchair domain wall. Here, we illustrate the tuning of the \mathbf{K} - \mathbf{K}' -valley hybridization using a tight-binding model. In this model, the quantum spin Hall and quantum valley Hall effects are implemented on a honeycomb lattice with the Kane-Mele model [32] and a staggered on-site potential [33], respectively. All parameters are determined according to the band structure of the corresponding PhCs (see the Supplementary Materials for details). In this idealized model, there is no inter-valley scattering along the unperturbed ($\epsilon = 0$) armchair domain wall, and the spin up (down) edge modes are doubly degenerate. To introduce inter-valley scattering, we perturb the armchair domain wall by applying the on-site potential $-\epsilon$ on the atomic sites along the armchair domain wall. This perturbation hybridizes the valley-polarized modes $\Psi_{\mathbf{K}(\mathbf{K}')\uparrow}$ to $\Psi_{\pm\uparrow}$ (Fig. 2). The energy-splitting between the two hybridized modes, $\Delta \equiv \omega_{+\uparrow} - \omega_{-\uparrow}$, increases linearly with $|\epsilon|$. Specifically, when $|\epsilon| \approx 0.42|t|$, $\Delta = \Delta_0$, where $\Delta_0 \approx 1.1 \times 10^{-2}(2\pi c/a_0)$ and t is the nearest-neighbor hopping.

The tunable \mathbf{K} - \mathbf{K}' -valley coupling at the armchair do-

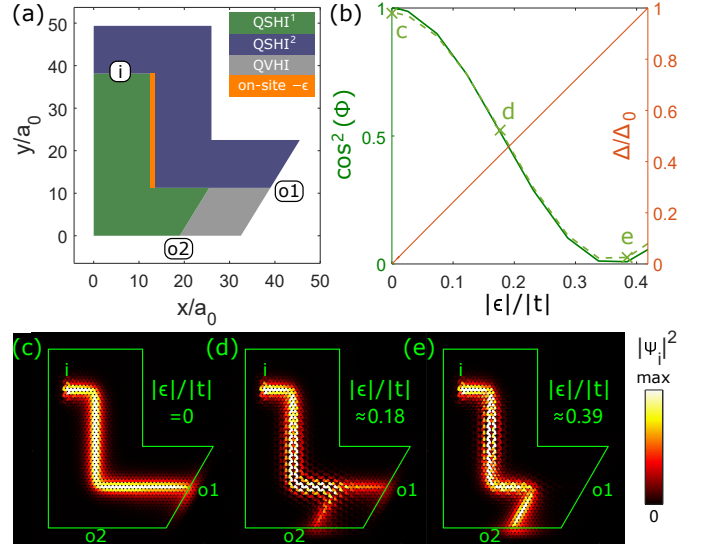


FIG. 3. Tight-binding simulation of the tunable Rabi oscillation. (a) Schematic of the tight-binding model. The green (blue) region represents QSHIs¹⁽²⁾ with clockwise (counterclockwise) next nearest neighbor hopping. The gray region represents the QVHI. The orange line along the armchair domain wall represents the atomic sites that experience the perturbation $-\epsilon$. (b) Analytical (solid line) and tight-binding (dashed line) results of tuning the \mathbf{K} -valley proportion in the output by varying the band-splitting Δ . Δ_0 corresponds to the inter-valley scattering with $|\epsilon| \approx 0.42|t|$ along the armchair domain wall. (c-e) Field profiles of Rabi oscillations with different inter-valley scattering Δ . After exiting the coupling region (armchair domain wall), the state becomes (c) \mathbf{K} -valley polarized, $P_{\mathbf{K}\uparrow}^{\text{TB}} : P_{\mathbf{K}'\uparrow}^{\text{TB}} \approx 1 : 0$; (d) equally \mathbf{K} - and \mathbf{K}' -valley polarized, $P_{\mathbf{K}\uparrow}^{\text{TB}} : P_{\mathbf{K}'\uparrow}^{\text{TB}} \approx 0.5 : 0.5$; (e) \mathbf{K}' -valley polarized, $P_{\mathbf{K}\uparrow}^{\text{TB}} : P_{\mathbf{K}'\uparrow}^{\text{TB}} \approx 0 : 1$.

main wall manifests itself when we measure the proportions $P_{\mathbf{K}\uparrow}$ and $P_{\mathbf{K}'\uparrow}$ after the Rabi oscillation. In the tight-binding simulation, we judiciously implemented a source that excites the $\Psi_{\mathbf{K}\uparrow}$ state only. $P_{\mathbf{K}\uparrow}$ and $P_{\mathbf{K}'\uparrow}$ are calculated using the squared amplitude $|\psi|^2$ at the output ports of the two single-mode valley-polarized waveguides, o1 and o2, according to the valley polarization that each waveguide selects: $P_{\mathbf{K}(\mathbf{K}')\uparrow}^{\text{TB}} \equiv \sum_{i \in \text{o1(o2)}} |\psi_i|^2 / \sum_{i \in \{\text{o1}, \text{o2}\}} |\psi_i|^2$. When $|\epsilon| = 0$, inter-valley scattering is completely suppressed ($\Delta = 0$), and the valley DoF is conserved. In this case, almost all the energy is directed to output port o1 and $P_{\mathbf{K}\uparrow}^{\text{TB}} : P_{\mathbf{K}'\uparrow}^{\text{TB}} \approx 1 : 0$, confirming that the output state is \mathbf{K} -valley polarized (Fig. 3c). When $|\epsilon| \approx 0.18|t|$, $\Phi(\Delta) \approx \pi/4$ in Eq. 2, and the output state has equal valley proportions, $P_{\mathbf{K}\uparrow}^{\text{TB}} : P_{\mathbf{K}'\uparrow}^{\text{TB}} \approx 0.5 : 0.5$ (Fig. 3d). Finally, when $|\epsilon| \approx 0.39|t|$, the inter-valley scattering at the armchair domain wall becomes large enough to result in $\Phi(\Delta) \approx \pi/2$, completely flipping the valley polarization from \mathbf{K} to \mathbf{K}' . Consequently, the output is \mathbf{K}' -valley polarized, $P_{\mathbf{K}\uparrow}^{\text{TB}} : P_{\mathbf{K}'\uparrow}^{\text{TB}} \approx 0 : 1$ (Fig. 3e). The tight-binding

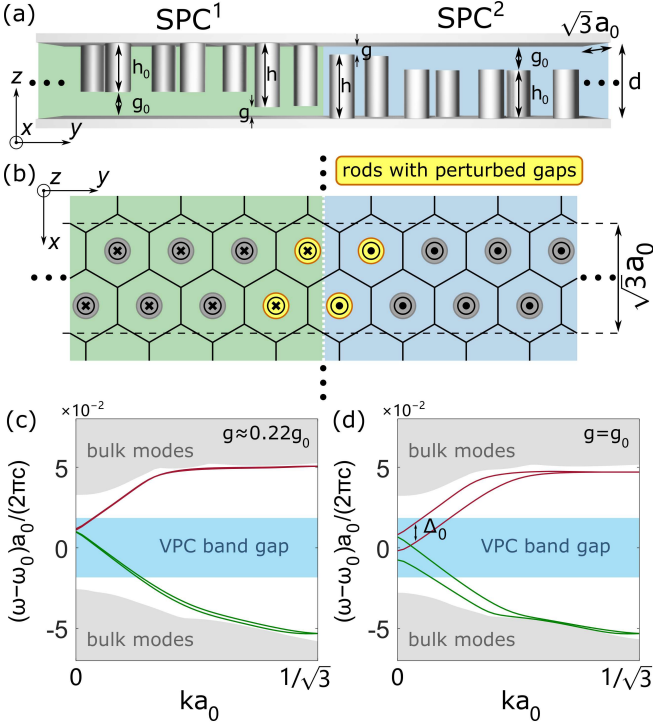


FIG. 4. (a,b) The photonic implementation of the armchair domain wall between QSHI^{1,2} using SPC^{1,2}. The gaps g adjacent to the domain wall are perturbed. (c,d) Photonic edge modes supported by the armchair domain wall with (c) $g \approx 0.22g_0$ and (d) $g = g_0$. Parameters of SPC^{1,2}: $g_0 = 0.15a_0$ is the height of unperturbed gaps; $h_0 = 0.85a_0$, $d = a_0$, where a_0 is the lattice constant. The mid-gap frequency of the VPC band gap is $\omega_0 \approx 0.75(2\pi c/a_0)$.

model hence confirms that one type of perturbation along the armchair domain wall tunes the inter-valley scattering, and the setup in Fig. 3a can be viewed as a lattice model of a tunable TDC.

To introduce tunability in the photonic implementation of the TDC (Fig. 1), we use the height of the gaps between the rods and the top (bottom) plate and most adjacent to the domain wall, g (Fig. 4a), as the control knob for manipulating the \mathbf{K} - \mathbf{K}' -valley scattering because the electromagnetic field of edge modes is exponentially localized at the domain wall and predominantly concentrated in those gaps. By extending the cavity perturbation theory to incorporate multimodal interactions [34, 35], we find that the effects of perturbing those gaps are mostly confined to each spin subspace – the spin DoF is largely conserved when the valleys are hybridized (see the Supplementary Material for details). When $g \approx 0.22g_0$, the inter-valley scattering is negligible, corresponding to $\Delta \approx 0$ (Fig. 4c). As g increases, the inter-valley scattering is enhanced. When $g = g_0$, the inter-valley scattering at the armchair domain wall causes a strong \mathbf{K} - \mathbf{K}' -valley hybridization with the splitting $\Delta = \Delta_0$ (Fig. 4d) (Note that Δ_0 shares the same

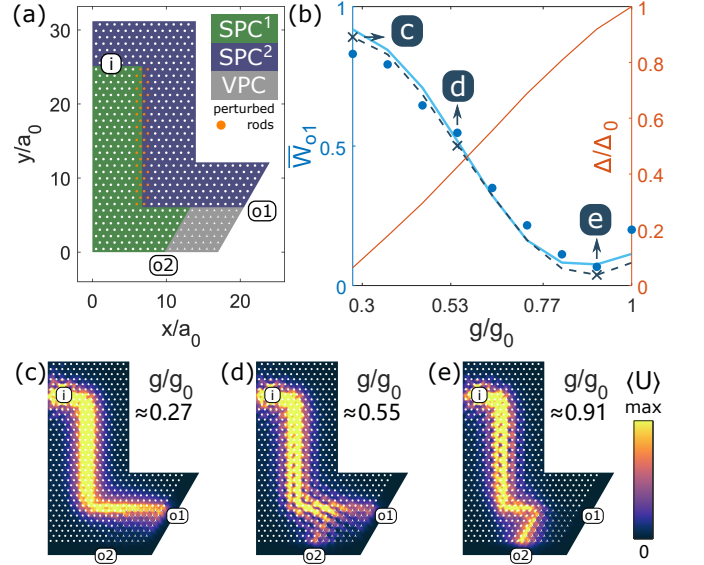


FIG. 5. The experimental implementation and electromagnetic simulation of the TDC. (a) Schematic of the TDC based on topological PhCs. Blue (green) region: SPC² (SPC¹); Gray region: VPC. Orange dots along the armchair domain wall: rods with the perturbed gaps g . (b) Semi-analytical (solid line), simulation (dashed line), and experiment (dots) results of the electromagnetic energy ratio received at output port o1. \overline{W}_{o1} is associated with the \mathbf{K} -valley polarization. Δ_0 corresponds to the inter-valley scattering with $g = g_0$ in Fig. 4a. The experimental data is averaged over the frequency range $\omega_0 < \omega < 1.022\omega_0$, where back-reflection is suppressed (see Supplementary Material for details). (c-e) COMSOL simulation of the beam splitting with three different g values at $\omega \approx 1.01\omega_0$: (c) $W_{o1} : W_{o2} \approx 0.89 : 0.11$; (d) $W_{o1} : W_{o2} \approx 0.50 : 0.50$; (e) $W_{o1} : W_{o2} \approx 0.04 : 0.96$.

value obtained from the tight-binding model with the perturbation setting $|\epsilon| \approx 0.42|t|$.)

The experimental implementation of the TDC was carried out in the microwave regime with $a_0 = 36.8\text{mm}$ (see Fig. 4 for other parameters). We increase the \mathbf{K} - \mathbf{K}' -valley hybridization by incrementing g from $0.27g_0$ to g_0 . We calculate the proportions of the valley polarizations, $P_{\mathbf{K}\uparrow}$ and $P_{\mathbf{K}'\uparrow}$, using the electromagnetic field energy at output ports o1 and o2: $P_{\mathbf{K}(\mathbf{K}')\uparrow}^{\text{exp}} = \overline{W}_{o1(o2)} \equiv W_{o1(o2)} / \sum_{i \in \{1,2\}} W_{oi}$. Experimental results demonstrate that, as the gap height g increases, $P_{\mathbf{K}\uparrow}^{\text{exp}} : P_{\mathbf{K}'\uparrow}^{\text{exp}}$ changes from $0.83 : 0.17$ to $0.07 : 0.93$, agreeing with COMSOL simulations (Fig. 5b-e). In contrast to the tight-binding model, $P_{\mathbf{K}\uparrow} : P_{\mathbf{K}'\uparrow}$ of the photonic structure does not reach $1 : 0$ and $0 : 1$. Two factors give rise to this phenomenon: the imperfectness of the source and the finite dimension of the structure. The excited state is not exactly \mathbf{K} -valley-polarized, instead, the excitation efficiency ratio is $\eta_{\mathbf{K}\uparrow} / \eta_{\mathbf{K}'\uparrow} \approx 43$ for the realistic source. On the other hand, due to the finite dimension of the VPC, the detection antenna at output port o1 not only receives the transmitted $\Psi_{\mathbf{K}\uparrow}$ but also the evanescent tail

of the tunneled $\Psi_{\mathbf{K}'\uparrow}$. Taking both factors into consideration, our semi-analytical model extending Eq. 2 agrees with both simulation and experiment (see the Supplementary Material and Ref. [25] for details).

We have demonstrated a tunable TDC based on tuning the valley-hybridization of edge states via relaxing the topological protection of the valley DoF. With additional delay lines, any arbitrary U(2) operation on the valley-polarized states can be realized using SPC^{1,2} and VPC as elementary building components (see Supplementary Material for details). When the valley-hybridization is tuned, the spin DoF stays conserved for a wide range of frequency (from ω_0 to $1.022\omega_0$, about 50% of the VPC band gap width), and the guided modes remain immune to back-scattering while turning around 90° corners, keeping the structure compact. Moreover, because the edge states supported by the multi-mode waveguiding domain wall originate from the Dirac cones gapped through the same mechanism, they propagate at identical group velocities across the topological band gap, potentially accommodating more complicated light flow manipulations.

Our design offers a new way for developing interferometers – through breaking the protection of one specific topological DoF, the corresponding edge modes are coupled. This paradigm offers a control knob from first principles for adjusting the coupling: the extent of topological-protection-breaking. Therefore, our design is fundamentally different from conventional directional couplers, for which mode hybridization is due to the evanescent coupling of the two waveguide modes and usually tuned by empirically adjusting the waveguide geometry and separation [36]. Additionally, TDCs can scale up with a cascading architecture, similar to MZI meshes. Compared to interferometers based on single-mode topological waveguides [21], our design harnesses the multimodeness and offers controllability via carefully relaxing the valley conservation, both of which could enable applications in microwave metamaterials and quantum computing [37, 38]. With all-dielectric SPCs and VPCs for the telecommunication spectrum [31, 39], the same design can possibly be realized on chip and combined with other topological photonic components [30, 39–41], allowing future progress in integrated photonics, photonic neuromorphic computing, and programmable quantum circuits [42–44].

REFERENCES

- [1] Yichen Shen, Nicholas C. Harris, Scott Skirlo, Mihika Prabhu, Tom Baehr-Jones, Michael Hochberg, Xin Sun, Shijie Zhao, Hugo Larochelle, Dirk Englund, and Marin Soljačić. Deep learning with coherent nanophotonic circuits. *Nature Photonics*, 11(7):441–446, Jul 2017.
- [2] Nicholas C. Harris, Gregory R. Steinbrecher, Mihika Prabhu, Yoav Lahini, Jacob Mower, Darius Bunandar, Changchen Chen, Franco N. C. Wong, Tom Baehr-Jones, Michael Hochberg, Seth Lloyd, and Dirk Englund. Quantum transport simulations in a programmable nanophotonic processor. *Nature Photonics*, 11(7):447–452, Jul 2017.
- [3] J. M. Arrazola, V. Bergholm, K. Brádler, T. R. Bromley, M. J. Collins, I. Dhand, A. Fumagalli, T. Gerrits, A. Goussev, L. G. Helt, J. Hundal, T. Isacsson, R. B. Israel, J. Izaac, S. Jahangiri, R. Janik, N. Killoran, S. P. Kumar, J. Lavoie, A. E. Lita, D. H. Mahler, M. Menotti, B. Morrison, S. W. Nam, L. Neuhaus, H. Y. Qi, N. Quesada, A. Repeating, K. K. Sabapathy, M. Schuld, D. Su, J. Swinerton, A. Száva, K. Tan, P. Tan, V. D. Vaidya, Z. Vernon, Z. Zabaneh, and Y. Zhang. Quantum circuits with many photons on a programmable nanophotonic chip. *Nature*, 591(7848):54–60, Mar 2021.
- [4] Michael Reck, Anton Zeilinger, Herbert J. Bernstein, and Philip Bertani. Experimental realization of any discrete unitary operator. *Phys. Rev. Lett.*, 73:58–61, Jul 1994.
- [5] Pieter Kok, W. J. Munro, Kae Nemoto, T. C. Ralph, Jonathan P. Dowling, and G. J. Milburn. Linear optical quantum computing with photonic qubits. *Rev. Mod. Phys.*, 79:135–174, Jan 2007.
- [6] William R. Clements, Peter C. Humphreys, Benjamin J. Metcalf, W. Steven Kolthammer, and Ian A. Walmsley. Optimal design for universal multiport interferometers. *Optica*, 3(12):1460–1465, Dec 2016.
- [7] Jacques Carolan, Christopher Harrold, Chris Sparrow, Enrique Martín-López, Nicholas J. Russell, Joshua W. Silverstone, Peter J. Shadbolt, Nobuyuki Matsuda, Manabu Oguma, Mikitaka Itoh, Graham D. Marshall, Mark G. Thompson, Jonathan C. F. Matthews, Toshikazu Hashimoto, Jeremy L. O’Brien, and Anthony Laing. Universal linear optics. *Science*, 349(6249):711–716, 2015.
- [8] Je-Hyung Kim, Shahriar Aghaeimeibodi, Jacques Carolan, Dirk Englund, and Edo Waks. Hybrid integration methods for on-chip quantum photonics. *Optica*, 7(4):291–308, Apr 2020.
- [9] Wim Bogaerts, Daniel Pérez, José Capmany, David A. B. Miller, Joyce Poon, Dirk Englund, Francesco Morichetti, and Andrea Melloni. Programmable photonic circuits. *Nature*, 586(7828):207–216, Oct 2020.
- [10] Menno Poot, Carsten Schuck, Xiao song Ma, Xiang Guo, and Hong X. Tang. Design and characterization of integrated components for silicon photonic quantum circuits. *Opt. Express*, 24(7):6843–6860, Apr 2016.
- [11] Ling Lu, John D. Joannopoulos, and Marin Soljačić. Topological photonics. *Nature Photonics*, 8(11):821–829, Nov 2014.
- [12] Alexander B. Khanikaev and Gennady Shvets. Two-dimensional topological photonics. *Nature Photonics*, 11(12):763–773, Dec 2017.
- [13] Tomoki Ozawa, Hannah M. Price, Alberto Amo, Nathan Goldman, Mohammad Hafezi, Ling Lu, Mikael C. Rechtsman, David Schuster, Jonathan Simon, Oded Zeitlinger, and Iacopo Carusotto. Topological photonics.

* yl2695@cornell.edu

† gshvets@cornell.edu

- Rev. Mod. Phys.*, 91:015006, Mar 2019.
- [14] Zheng Wang, Yidong Chong, J. D. Joannopoulos, and Marin Soljačić. Observation of unidirectional backscattering-immune topological electromagnetic states. *Nature*, 461(7265):772–775, Oct 2009.
- [15] Alexander B. Khanikaev, S. Hossein Mousavi, Wang-Kong Tse, Mehdi Kargarian, Allan H. MacDonald, and Gennady Shvets. Photonic topological insulators. *Nature Materials*, 12(3):233–239, Mar 2013.
- [16] Konstantin Y. Bliokh, Daria Smirnova, and Franco Nori. Quantum spin hall effect of light. *Science*, 348(6242):1448–1451, 2015.
- [17] Jiho Noh, Sheng Huang, Kevin P. Chen, and Mikael C. Rechtsman. Observation of photonic topological valley hall edge states. *Phys. Rev. Lett.*, 120:063902, Feb 2018.
- [18] Andrea Blanco-Redondo, Bryn Bell, Dikla Oren, Benjamin J. Eggleton, and Mordechai Segev. Topological protection of biphoton states. *Science*, 362(6414):568–571, 2018.
- [19] Michelle Wang, Cooper Doyle, Bryn Bell, Matthew J. Collins, Eric Magi, Benjamin J. Eggleton, Mordechai Segev, and Andrea Blanco-Redondo. Topologically protected entangled photonic states. *Nanophotonics*, 8(8):1327–1335, 2019.
- [20] Sunil Mittal, Elizabeth A. Goldschmidt, and Mohammad Hafezi. A topological source of quantum light. *Nature*, 561(7724):502–506, Sep 2018.
- [21] Yang Chen, Xin-Tao He, Yu-Jie Cheng, Hao-Yang Qiu, Lan-Tian Feng, Ming Zhang, Dao-Xin Dai, Guang-Can Guo, Jian-Wen Dong, and Xi-Feng Ren. Topologically protected valley-dependent quantum photonic circuits. *Phys. Rev. Lett.*, 126:230503, Jun 2021.
- [22] Herbert Kroemer. Nobel lecture: Quasielectric fields and band offsets: teaching electrons new tricks. *Rev. Mod. Phys.*, 73:783–793, Oct 2001.
- [23] Motohiko Ezawa. Topological kirchhoff law and bulk-edge correspondence for valley chern and spin-valley chern numbers. *Phys. Rev. B*, 88:161406, Oct 2013.
- [24] Tzuhsuan Ma and Gennady Shvets. Scattering-free edge states between heterogeneous photonic topological insulators. *Phys. Rev. B*, 95:165102, Apr 2017.
- [25] Yandong Li, Yang Yu, Kueifu Lai, Yuchen Han, Fei Gao, Baile Zhang, and Gennady Shvets. Mode-selective single-dipole excitation and controlled routing of guided waves in a multi-mode topological waveguide. *Applied Physics Letters*, 120(22):221702, 2022.
- [26] Tzuhsuan Ma and Gennady Shvets. All-si valley-hall photonic topological insulator. *New Journal of Physics*, 18(2):025012, feb 2016.
- [27] Fei Gao, Haoran Xue, Zhaoju Yang, Kueifu Lai, Yang Yu, Xiao Lin, Yidong Chong, Gennady Shvets, and Baile Zhang. Topologically protected refraction of robust kink states in valley photonic crystals. *Nature Physics*, 14(2):140–144, Feb 2018.
- [28] Kyoko Nakada, Mitsutaka Fujita, Gene Dresselhaus, and Mildred S. Dresselhaus. Edge state in graphene ribbons: Nanometer size effect and edge shape dependence. *Phys. Rev. B*, 54:17954–17961, Dec 1996.
- [29] L. Brey and H. A. Fertig. Electronic states of graphene nanoribbons studied with the dirac equation. *Phys. Rev. B*, 73:235411, Jun 2006.
- [30] Yandong Li, Yang Yu, Fengyu Liu, Baile Zhang, and Gennady Shvets. Topology-controlled photonic cavity based on the near-conservation of the valley degree of freedom. *Phys. Rev. Lett.*, 125:213902, Nov 2020.
- [31] Yuhao Kang, Xiang Ni, Xiaojun Cheng, Alexander B. Khanikaev, and Azriel Z. Genack. Pseudo-spin–valley coupled edge states in a photonic topological insulator. *Nature Communications*, 9(1):3029, Aug 2018.
- [32] C. L. Kane and E. J. Mele. Quantum spin hall effect in graphene. *Phys. Rev. Lett.*, 95:226801, Nov 2005.
- [33] Gordon W. Semenoff. Condensed-matter simulation of a three-dimensional anomaly. *Phys. Rev. Lett.*, 53:2449–2452, Dec 1984.
- [34] J. C. Slater. Microwave electronics. *Rev. Mod. Phys.*, 18:441–512, Oct 1946.
- [35] George E. Dombrowski. Matrix formulation of Slater’s cavity perturbation theorem. *Journal of Applied Physics*, 55(7):2648–2650, 04 1984.
- [36] Andrea Crespi, Roberto Osellame, Roberta Ramponi, Daniel J. Brod, Ernesto F. Galvão, Nicolò Spagnolo, Chiara Vitelli, Enrico Maiorino, Paolo Mataloni, and Fabio Sciarrino. Integrated multimode interferometers with arbitrary designs for photonic boson sampling. *Nature Photonics*, 7(7):545–549, Jul 2013.
- [37] Lianlin Li, Hanting Zhao, Che Liu, Long Li, and Tie Jun Cui. Intelligent metasurfaces: control, communication and computing. *eLight*, 2(1):7, May 2022.
- [38] Xiu Gu, Anton Frisk Kockum, Adam Miranowicz, Yu xi Liu, and Franco Nori. Microwave photonics with superconducting quantum circuits. *Physics Reports*, 718–719:1–102, 2017. Microwave photonics with superconducting quantum circuits.
- [39] Mikhail I. Shalaev, Wiktor Walasik, Alexander Tsukernik, Yun Xu, and Natalia M. Litchinitser. Robust topologically protected transport in photonic crystals at telecommunication wavelengths. *Nature Nanotechnology*, 14(1):31–34, Jan 2019.
- [40] Sabyasachi Barik, Aziz Karasahin, Sunil Mittal, Edo Waks, and Mohammad Hafezi. Chiral quantum optics using a topological resonator. *Phys. Rev. B*, 101:205303, May 2020.
- [41] Yongquan Zeng, Udvas Chattopadhyay, Bofeng Zhu, Bo Qiang, Jinghao Li, Yuhao Jin, Lianhe Li, Alexander Giles Davies, Edmund Harold Linfield, Baile Zhang, Yidong Chong, and Qi Jie Wang. Electrically pumped topological laser with valley edge modes. *Nature*, 578(7794):246–250, Feb 2020.
- [42] Gordon Wetzstein, Aydogan Ozcan, Sylvain Gigan, Shanhui Fan, Dirk Englund, Marin Soljačić, Cornelia Denz, David A. B. Miller, and Demetri Psaltis. Inference in artificial intelligence with deep optics and photonics. *Nature*, 588(7836):39–47, Dec 2020.
- [43] Jianwei Wang, Fabio Sciarrino, Anthony Laing, and Mark G. Thompson. Integrated photonic quantum technologies. *Nature Photonics*, 14(5):273–284, May 2020.
- [44] Emanuele Pelucchi, Giorgos Fagas, Igor Aharonovich, Dirk Englund, Eden Figueroa, Qihuang Gong, Hübel Hannes, Jin Liu, Chao-Yang Lu, Nobuyuki Matsuda, Jian-Wei Pan, Florian Schreck, Fabio Sciarrino, Christine Silberhorn, Jianwei Wang, and Klaus D. Jöns. The potential and global outlook of integrated photonics for quantum technologies. *Nature Reviews Physics*, 4(3):194–208, Mar 2022.